Available online at www.sciencedirect.com

ScienceDirect

Polar Science 8 (2014) 57–72

http://ees.elsevier.com/polar/

Case study on microphysical properties of boundary layer mixed-phase cloud observed at Ny-Ålesund, Svalbard: Observed cloud microphysics and calculated optical properties on 9 June 2011

Akihiro Uchiyama [a,*], Akihiro Yamazaki [a], Masataka Shiobara [b], Hiroshi Kobayashi [c]

[a] *Japan Meteorological Agency Meteorological Research Institute, Nagaimine, Tsukuba 305-0052, Japan*
[b] *National Institute of Polar Research, Midoricho, Tachikawa, Tokyo 190-8518, Japan*
[c] *University of Yamanashi, Takeda, Kofu, Yamanashi 400-8510, Japan*

Received 13 March 2013; revised 22 October 2013; accepted 1 November 2013
Available online 15 November 2013

Abstract

Cloud radiation interactions are important in the global climate system. However, an understanding of mixed-phase boundary layer clouds in the Arctic remains poor. During May–June 2011, ground-based in situ measurements were made at Zeppelin Station, operated by the Norwegian Polar Institute (altitude 474 m) in Ny-Ålesund (78.9°N, 11.9°E), Svalbard. The instruments used comprised a Cloud, Aerosol and Precipitation Spectrometer (CAPS), and a Cloud Particle Microscope imager. The CAPS incorporated a Cloud and Aerosol Spectrometer and Cloud Imaging Probe (CIP). During the observation period, clouds associated with cyclonic disturbances and those associated with outbreaks of westerly cold air masses from the sea were observed. Atmospheric temperature during all measurements ranged from 0 to −5 °C. In every case, columns were the major type of ice particle measured by the CAPS–CIP. Cloud microphysical properties were observed continuously on 9 June 2011. Size spectra, liquid/ice water content, and particle effective size changed depending on progress stages. Based on the observed microphysics, optical properties were calculated and investigated. Optical properties were determined mainly by those of liquid water particles, even during periods when the relative contribution of ice particles to total water content was at the maximum. It was confirmed that the wavelength region of 1.6 and 2.2 μm can be used in remote sensing. This study shows that it is possible to measure detailed changes of cloud properties in the Arctic region by using instruments installed at a ground-based mountain station.

Keywords: Boundary layer; Mixed-phase cloud; Microphysical properties; Optical properties

1. Introduction

The earth radiation budget is an important factor in the climate system, in which clouds play a crucial role. In the Arctic region, it is generally known that clouds have a seasonal cycle with minima in early spring and maxima in late summer (Shupe et al., 2011). Low-level, mixed-phase clouds are observed most frequently during the spring and autumn transition season (Shupe et al., 2006). These mixed-phase clouds are important in the Arctic surface radiation budget, owing to their large horizontal extent and persistence (Shupe and Intrieri, 2004; Zuidema et al., 2005).

* Corresponding author. Tel.: +81 298538605; fax: +81 298552552.
E-mail address: uchiyama@mri-jma.go.jp (A. Uchiyama).

1873-9652/$ - see front matter © 2013 Elsevier B.V. and NIPR. All rights reserved.
http://dx.doi.org/10.1016/j.polar.2013.11.001

In the Arctic region, the rate of the warming is more rapid than the global average and this is predicted to continue in the future (Solomon et al., 2007). However, climate model predictions vary considerably, owing to the complexity of the various climate feedback mechanisms and the scarcity of the data required for their study. In particular, differences in climate model representations of cloud are thought to be the main cause for the spread of Arctic predictions (Inoue et al., 2006; Gorodetskaya et al., 2008; Holland et al., 2008). Sensitive feedback mechanisms include the interaction of clouds with the typically high surface albedo of ice-covered Arctic regions, and with aerosols, radiation, cloud water content, and cloud drop size (Curry et al., 1996). Therefore, detailed measurements are a key requirement for improving knowledge of the complex interactions between the different physical processes, and for enhancing the microphysical and radiation parameterizations for Arctic climate models.

Several field experiments have been performed in recent decades. These include the Surface Heat Budget of the Arctic Ocean (SHEBA; Perovich et al., 1999), the International Satellite Cloud Climatology Project (ISCCP), the First ISCCP Regional Experiment – Arctic Cloud Experiment (FIRE ACE; Curry et al., 2000), the Arctic Study of Tropospheric Aerosol and Radiation (ASTAR; Yamanouchi et al., 2005), the Study of Environmental Arctic Change (SEARCH; SEARCH SSC, 2001), the Mixed-Phase Arctic Clouds Experiment (MPACE; Verlinde et al., 2007), the Aerosol, Radiation, and Cloud Processes affecting Arctic Climate project (ARCPAC, Brock et al., 2011), and the Indirect and Semi-Direct Aerosol Campaign (ISDAC; McFarquhar et al., 2011).

In this paper, we describe the observational results from clouds formed in the vicinity of Ny-Ålesund, Svalbard. Clouds in this area have been observed by Gayet et al. (2007, 2009) using aircraft and remote sensing instruments. Campbell and Shiobara (2008) reported on the glaciation process of a mixed-phase cloud at Ny-Ålesund after natural seeding by ice crystals. They used a Micro Pulse Lidar (MPL) that measures clouds remotely from the surface. The unique aspect of our observations is that in situ measurements of cloud microphysics were made at a ground-based site using instruments designed for airborne measurements, and that these measurements enabled us to observe clouds continuously for long periods.

Such an observation was performed on 9 June 2011, and we present the results herein. Cloud microphysical properties were investigated using these data, and optical properties were calculated and explored. In Section 2, the observation site, period of observation, and the instrumentation are described. In Section 3, we address the processing of particle image data and the empirical formulae used to calculate the physical properties of the clouds. In Section 4, the meteorological conditions, observational results of the cloud microphysics, and the optical properties deduced from the measured cloud microphysics are described. The summary and conclusions are presented in Section 5.

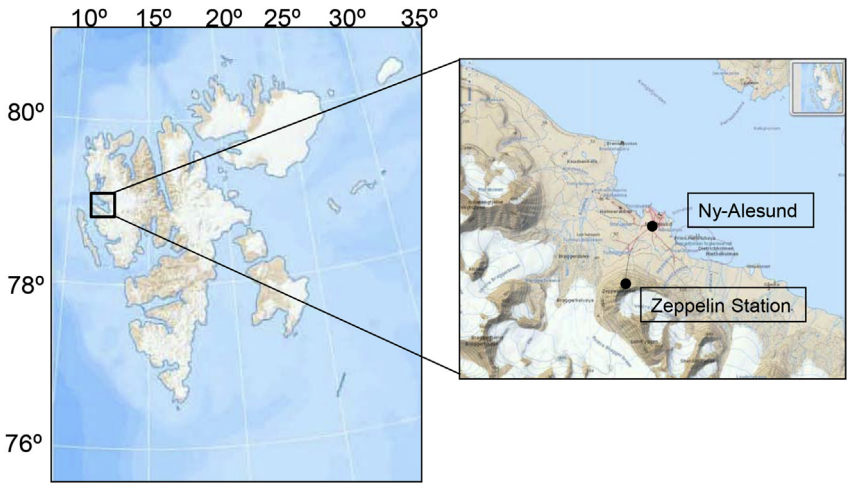

Fig. 1. Location of ground-based, in situ measurements at Zeppelin Station of Norwegian Polar Institute (altitude 474 m) in Ny-Ålesund (78.9°N, 11.9°E), Svalbard.

2. Method

2.1. Observation site and period

The instruments were installed on the roof at Zeppelin Station in Ny-Ålesund (78.9°N, 11.9°E). This station is operated by the Norwegian Polar Institute. It is located at an altitude of 474 m, near the peak of Mt. Zeppelin (Fig. 1).

Boundary layer mixed-phase clouds in the Svalbard vicinity, such as those described here, cover considerable areas and persist for several days. Generally, they are observed during spring and autumn and are related to cold air outbreaks from northern ice fields (Kolstad et al., 2008; Richter et al., 2008). Shiobara et al. (2003) showed that these boundary layer clouds often have a cloud base height (CBH) below 2000 m during spring to late summer. Therefore, given its elevation, Zeppelin Station is likely to encounter such clouds. After installing the instruments, we began observations on 13 May 2011 and ended on 10 June 2011. However, owing to the weather conditions, we could only take measurements from 1 to 10 June. CBHs were higher than the observation site, and there were long periods of days with fine weather.

2.2. Instruments

The instruments consisted of a Cloud, Aerosol and Precipitation Spectrometer (CAPS, Droplet Measurement Technologies), a Gerber Particulate Volume Monitor (PVM-100, Gerber Scientific Inc.), and a Cloud Particle Microscope (CPM) imager (Fig. 2).

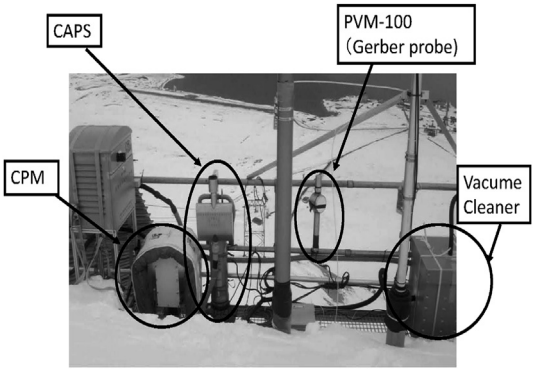

Fig. 2. Instruments installed on roof of Zeppelin Station. These were Cloud, Aerosol and Precipitation Spectrometer (CAPS), Gerber Particulate Volume Monitor (PVM-100), and Cloud Particle Microscope (CPM) imager. CAPS is composed of Cloud and Aerosol Spectrometer (CAS) and Cloud Imaging Probe (CIP).

These were designed for airborne measurements, except for the CPM.

The CAPS is manufactured by Droplet Measurement Technologies, and comprises a Cloud and Aerosol Spectrometer (CAS) and a Cloud Imaging Probe (CIP) (Baumgardner et al., 2002). The CAPS–CAS and CAPS–CIP have the same measurement capabilities as the Forward Scattering Spectrometer Probe (models 100 and 300), and the 2D optical array probe, respectively. They measure particles from 0.35 to 50 μm and 25 to 1550 μm in diameter, respectively.

The CAS measurement technique is similar to that of the Forward Scattering Spectrometer Probe-100, i.e., the collection of forward-scattered light (4–13°) from single particles passing through a focused laser beam. The CAS has an additional set of optics and detectors that measure backscattered light (5–14°). The size of each particle is determined using Mie scattering theory and by assuming spherical particles of given refractive index.

The CIP measures particle images by using the same technique as the Particle Measuring Systems Inc. 2D optical array probe, i.e., capturing the shadows of particles passing through a focused laser beam. A collimated laser beam from a diode laser is positioned on a linear array of 64 diodes. Each time the array moves a distance of 25 μm (the probe resolution) the on–off state of each diode is recorded as the particle image moves across the array.

As CAPS is an instrument designed for airborne measurements, airflow is required in front of the probe detector. An airflow guide was attached to the CAPS–CIP and sample air was drawn by a vacuum cleaner. Airflow rate was adjusted to about 10 m s^{-1}, under which conditions, the imaged water droplets became circular. Because the airflow guide is narrow, it was not necessary to consider crosswind components. The CAP–CAS also required airflow, for which a vacuum cleaner was affixed to its outlet, drawing sample air. The flow rate was adjusted to that of the CAPS–CIP.

The PVM-100 is intended for water clouds and is unsuitable for mixed-phase clouds. Therefore, data measured by the PVM-100 were not used.

The CPM was developed recently by one of the authors and improvements of the CPM are ongoing. It consists of a charge-coupled device camera and microscope, which takes images of cloud particles. Data measured by the CPM were not used for quantitative analysis. Instead, its images were used to determine whether the particles observed were water droplets or ice particles.

During the campaign, the continuous measurement by the MPL at the surface was useful for monitoring the CBH of low clouds over Ny-Ålesund. Details of the MPL are given in Shiobara et al. (2006).

3. Data processing

The size spectrum from 0.35 to 1550 μm in diameter was obtained from the CAPS–CAS and CAPS–CIP measurements. As shown in Fig. 3, size spectra measured by these instruments were connected to each other smoothly and had three distinctive peaks. We believe that these peaks reflect a difference of particle components. The peak around 0.4-μm radius corresponds to aerosols, that around 10 μm to water clouds, and that around 100 μm to ice clouds, which also contain large water droplets. The first channel in the CAPS–CAS may underestimate the number density, because statistics from the Zeppelin station (Tunved et al., 2013) did not show an indication of such drops. Particles larger than 2-μm radius measured by CAPS–CAS were regarded as water droplets. Particles measured by CAPS–CIP were considered a mixture of water droplets and ice particles. Once the size spectra for each particle type are known, liquid water content (LWC), ice water content (IWC), and optical properties can be determined by empirical parameterization formulae and theoretical calculation. In the following, data processing of CAPS–CIP images and the empirical formulae used herein are described.

3.1. Image data processing of CAPS–CIP

An example of images taken by the CAPS–CIP is shown in Fig. 4. The image includes various types of particles. Predominant particles are of the column-type, but circular objects and aggregated particles are also evident. Images that are more complex, such as those of bullet rosettes, are rare.

Generally, ice particles have complex shapes. Therefore, when images of ice particles are analyzed, a "circular" approximation is used (Heymsfield and Parrish, 1978), following which particle parameters are extracted. However, there are numerous column-type particles seen in the images taken in this study, as shown in Fig. 4. Therefore, a new method was developed to analyze column-type particles, in which an "elliptical" rather than a circular shape is assumed to extract particle shape parameters.

In particle image analysis, it is assumed that the ellipse area equals the shaded area of the particle. Furthermore, images with maximum dimension $\geq$3 elements ($\geq$75 μm) are analyzed, because shape distinction is difficult with smaller dimensions. The sampling volume is calculated assuming "center-in"; the center of the particle is in the actual sampling area. The method to calculate the sampling volume is described in detail by Heymsfield and Parrish (1978). In this study, because we processed the data that included a large portion of particles passing through the laser beam, "center-in" is assumed.

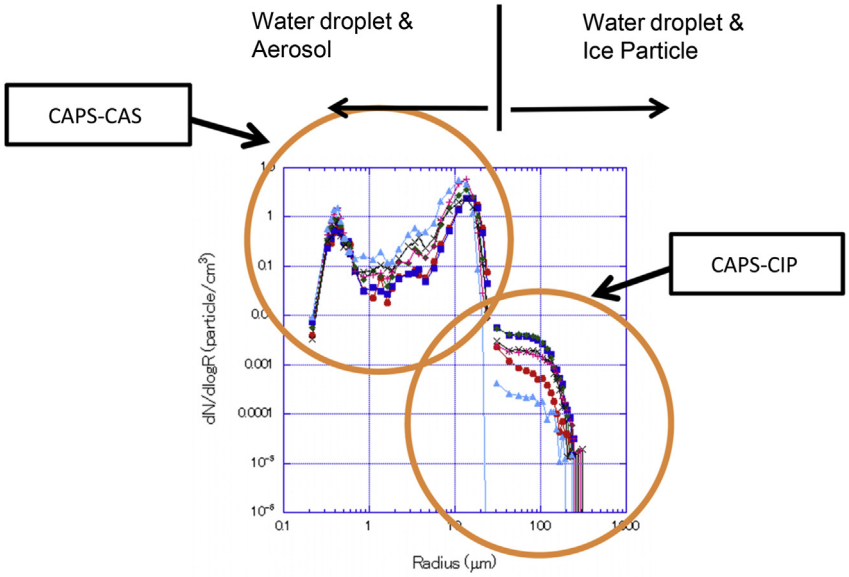

Fig. 3. Examples of particle size spectra measured by CAPS–CAS and CAPS–CIP between 08:00 and 11:00 on 9 June 2011. Aerosol particles and water droplets are measured by CAPS–CAS, and ice particles by CAPS–CIP.

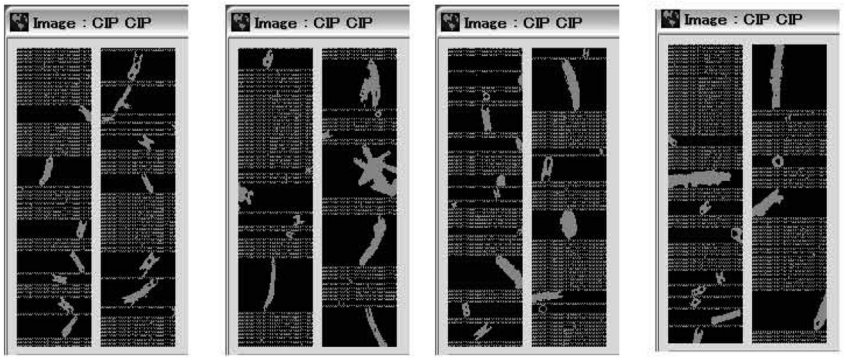

Fig. 4. Examples of CAPS–CIP images.

The particle images are analyzed by the following procedure. Before processing the image data, the following two rejection criteria are applied.

1) Particles with length of flow direction (Lf) $>$ 80 elements (2000 μm) are rejected.
2) Particles with $Ledge/Lp > 0.2$ are rejected, where Lp is the perimeter of the particle images including the edge element, and $Ledge$ is the length of the edge (where the edge is the 1st or 64th element). These parameters are shown in Fig. 5.

Water droplets very occasionally flow over the window of the CAPS–CIP probe, generating an elongated image in the direction of sample airflow. The first criterion rejects these images. When $Ledge/Lp$ is large, we cannot determine accurately the length of the major and minor axes of the ellipse. The second criterion ensures that a large proportion of particles pass through the laser beam and that particle centers are within the image.

The particle type is classified as a sphere, column, aggregate or other, based on the following parameters.

$$\text{Axis ratio} = b/a \tag{1}$$

$$\textit{Perimeter ratio} = Lp/Lc, \tag{2}$$

and

$$\text{Difference of perimeter} = Lcol/Lc - Lp/Lc, \tag{3}$$

where a and b are the lengths of the major and minor axes of the ellipse, respectively. Lc is the circumference of the equivalent area, and $Lcol = 2(a + b)$ is the perimeter of a rectangle with side lengths a and b. Using these parameters, the particle shape is classified according to Fig. 6. Parameter values were determined empirically by processing images of many types of artificial particle prior to processing the real observation data. The artificial particles, which have various kinds of shape and size, were tested against the standard classification: circular, column type, bullet rosettes, and aggregates.

3.2. Liquid/ice water content

Using data of size spectra and particle type, the LWCs and IWCs were calculated.

Spherical particles were regarded as water droplets, from which the LWC was calculated.

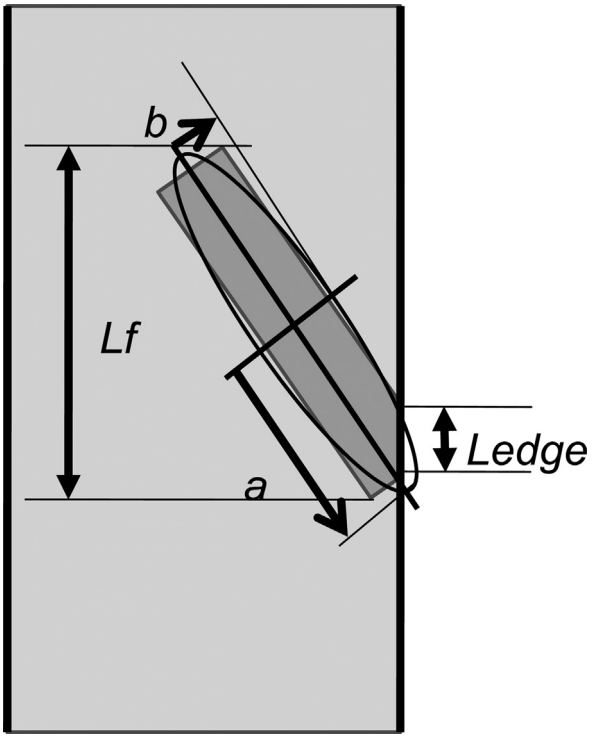

Fig. 5. Parameters of particle image. a and b are lengths of major and minor axes of ellipse. Lf is length of sample airflow direction. $Ledge$ is length of edge.

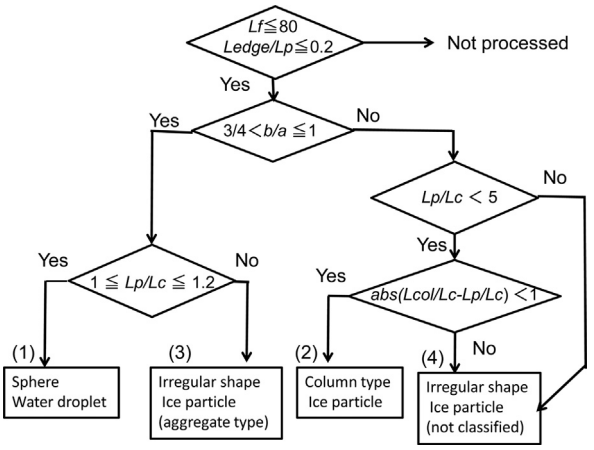

Fig. 6. Decision tree of cloud particle classification. Particles were classified as sphere, column, aggregate, and other (unclassified).

IWC was calculated by using particle shape parameters and empirical formulae. For column-type particles, the parameterization of Mitchell and Arnott (1994) was used. Using the data of Auer and Veal (1970), the volume and length of columnar ice crystals can be related. The volume V is

$$V = 0.00180L^{1.908} \quad \text{for } L \geq \quad 100\ \mu\text{m} \tag{4}$$

$$V = 0.1823L^{2.908} \quad \textit{for } L < 100\ \mu m, \tag{5}$$

where the units of L are cm and those of V are cm^3. The units used were the same as in the original papers to avoid mistakes of unit conversion.

The density is necessary to convert volume to IWC. We used the density in the warm region from Heymsfield (1972).

$$\rho_i = 0.848L^{-0.014} \quad \text{for} \quad L \geq \quad 0.014\ \text{mm}, \tag{6}$$

where ρ_i is density with units g cm^{-3}, and units of L are mm.

For ice particles, except the column type, the empirical formula of Cunningham (1978) was used. The equation and coefficients are shown in Table 1 of Boudala et al. (2002); those for irregularly shaped particles were used.

$$D_e = aA^b, \tag{7}$$

where D_e is the equivalent melted diameter, A is the projected area, and a and b are constants for a given habit. Units of A are mm^2 and those of D_e are mm.

$$a = 0.39,\ b = 0.31 \quad \text{for} \quad A \leq \quad 0.25\ \text{mm}^2, \tag{8}$$

$$a = 0.44,\ b = 0.4 \quad \textit{for} \quad A > \quad 0.25\ mm^2. \tag{9}$$

IWC of an ice particle with diameter D_e is

$$\text{IWC} = \frac{4}{3}\pi\rho_w\left(\frac{D_e}{2}\right)^3, \tag{10}$$

where ρ_w is the density of water.

3.3. Optical properties

The optical properties of ice particles were computed based on the database of Yang et al. (2000), using the parameters extracted from the measured images. Yang et al. (2000) computed single-scattering properties of ice crystals with various shapes and sizes in 56 narrow spectral bands from 0.2 to 5 μm. The ice crystal habits considered in their study were hexagonal plates, solid and hollow columns, planar and spatial bullet rosettes, and aggregates commonly observed in cirrus clouds. In the present study, we used the results of solid columns for particles classified as column-type, and of aggregates for particles classified as aggregate-type or other. For water droplets, single-scattering properties were calculated by Mie theory (Mie, 1908).

4. Results

4.1. Summary of observation (meteorological data)

After instrument installation on 13 May 2011, the first observation was made on 1 June 2011, followed by others through 10 June. During this period, there were clouds associated with cyclonic disturbances and with outbreaks of westerly cold air from the sea.

Table 1 lists the meteorological data. The meteorological data at Zeppelin station were measured by Norwegian Polar Institute and Norwegian Institute for Air Research. Wind at Zeppelin Station is affected by Mt. Zeppelin. We also show wind data from Alfred Wegener Institute, which is located at the foot of the mountain in central Ny-Ålesund town. As the wind in the town is also affected by the fjord, the wind observed by radiosonde is also shown in Table 2.

Apart from clouds associated with cyclonic disturbances, those associated with outbreaks of westerly cold air were observed frequently. We observed mixed-phase clouds with atmospheric temperature between −5 and 0 °C and relative humidity of 90–100% in every case. In the case of 9 June 2011, mixed-phase cloud was observed continuously from midnight until afternoon, and the change of cloud physical properties

Table 1
Summary of meteorological data.

Date	CAPS and CPM operation time	Meteorological situation	Cloud phase	Zeppelin station				Alfred Wegener Institute	
				Temp (°C)	RH (%)	Wind dir.	Wind speed (m s^{-1})	Wind dir.	Wind speed (m s^{-1})
2011/6/01	09:21:16–19:15:32	Clouds associated with cyclonic disturbance	Mixed phase cloud	−2–0	90–100	S	1–2	SW–SE	1–2
	19:59:39–23:59:58			−2	95–100	S	3–4	SE	1–2
2011/6/02	00:00:28–02:50:24	Clouds associated with cyclonic disturbance	Mixed phase cloud	−2–4	95–100	W	1–3	NW	4–7
	03:50:03–06:50:24			−3–4	95–100	S	0–1	NW	0–2
2011/6/04	15:23:21–18:08:02	Clouds associated with outbreak of westerly cold air	Predominantly liquid water cloud	−3–0	80–90	S	0–3	NW	3–4
2011/6/07	02:11:21–05:41:21	Clouds associated with outbreak of westerly cold air (orographic cloud)	Mixed phase cloud	−3	95–100	NW	2–3	SW–NW	1–3
2011/6/09	03:28:05–06:55:02	Clouds associated with outbreak of westerly cold air mass from the sea	Mixed phase cloud	−5–4	95–100	NW	0–3	WNW	4–6
	07:49:59–11:15:05			−5–3	95–100	NW	2	W	4–6
	12:11:46–13:50:03			−5–3	90	NW	2–4	WNW	6–8
2011/6/10	07:00:47–10:09:52	Clouds associated with outbreak of westerly cold air mass from the sea (dispersing)	Mixed phase cloud	−4–2	90–95	N–W	0.5–1	S–W	0–2

Meteorological situation was judged from satellite image, meteorological data and the direction of cloud movement.
Cloud phase was determined from the data measured by CAPS–CAS, CAPS–CIP and CPM.
The meteorological data at Zeppelin station were measured by Norwegian Polar Institute and Norwegian Institute for Air Research.
The meteorological data at Alfred Wegener Institute were measured by Alfred Wegener Institute.

Table 2
The meteorological data at 900 and 800 hPa measured by radiosonde launched from Alfred Wegener Institute.

Date		900 hPa				800 hPa			
		Temp. (°C)	RH (%)	Wind direction	Wind Speed (m s^{-1})	Temp. (°C)	RH (%)	Wind direction	Wind Speed (m s^{-1})
2011/06/01	12UTC	−2.8	99	189° (S)	5.5	−4.6	95	280° (W)	1.7
2011/06/02	12UTC	−5.8	89	208° (SSW)	5.3	−8.3	35	256° (WSW)	7.0
2011/06/04	12UTC	−5.0	89	210° (SSW)	2.9	−7.4	30	241° (WSW)	4.2
2011/06/07	12UTC	−4.8	86	14° (NEN)	1.9	−9.4	94	38° (NE)	7.4
2011/06/09	12UTC	−5.0	32	325° (NW)	3.9	−7.3	76	300° (WNW)	3.1
2011/06/10	12UTC	−3.3	65	35° (NE)	1.9	−4.6	51	286° (WNW)	5.6

was caught. The boundary layer cloud observed on this day moved from the west to the east direction, which was in the same direction as the wind observed at Alfred Wegener Institute. The wind direction measured by the radiosonde was 325° (NW) at 900 hPa and 300° (WNW) at 800 hPa. We focus on the observational results from this case.

4.2. Cloud properties

Observations on 9 June 2011 were conducted from 03:28 to 13:50 (local time), which was twice interrupted by data backup and instrument maintenance. This did not prevent the aforementioned continuous measurement, allowing us to observe the change of cloud properties. The instruments were installed on the roof of Zeppelin station and the measurements were performed at the ground-based fixed position. Therefore, we cannot distinguish the change in cloud properties caused by the movement of the cloud from that caused by the development of the cloud. Thus, we must interpret the change of observed data carefully.

Before we show the results of the physical properties observed, the change of cloud observed by the MPL is described below (Fig. 7).

The measurement began at around 03:30 (local time) when two cloud layers existed. The CBH of the lower cloud layer was 400–500 m. The CBH of the upper cloud layer was about 2 km and it was gradually lowering. The lidar signal from the lower cloud layer reached the ground after around 05:00. This meant that precipitation started from around 05:00. This precipitation was caused by seeding from the upper layer cloud. A similar phenomenon was observed by Campbell and Shiobara (2008). Thereafter, the upper layer cloud could not be detected clearly owing to the attenuation by the lower cloud layer and the precipitation. The precipitation from the lower cloud layer

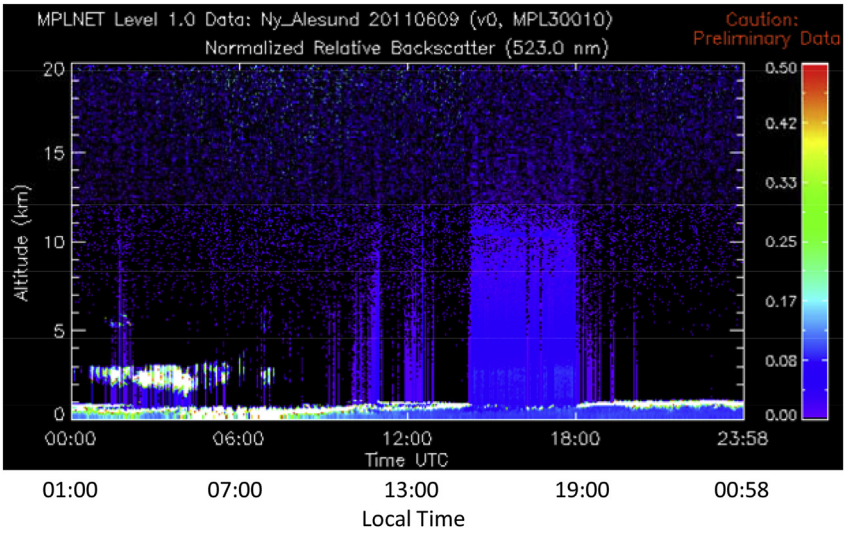

Fig. 7. MPLNET normalized relative backscatter data from 00:00 to 23:58 UTC 9 June 2011 at Ny-Ålesund.

stopped at around 07:30, by which time the upper cloud layer had dissipated. After the precipitation ceased, the dense lower cloud layer remained with constant CBH until about 10:00; its height was about 400 m. Thereafter, the CBH gradually lifted and the cloud layer became scattered. By about 14:30, the cloud layer had dissipated.

Fig. 8 shows the LWC and IWC. Fig. 9 depicts the relative contribution of particle types to the total water content (TWC), where TWC = LWC + IWC. The TWC increased gradually from 05:00 to 09:00 with some variation. The MPL data showed precipitation between 05:30 and 07:30. In the early period of precipitation, the TWC is small, whereas in the latter period of precipitation, the TWC was increasing gradually. The TWC became maximized from 09:00 to 10:00. In this period, according to the MPL data, the cloud layer was dense and stable. Thereafter, the TWC decreased gradually and became nearly zero by about 12:00, at which point the CBH was rising and the Zeppelin station emerged from the cloud layer. Furthermore, the cloud layer became increasingly scattered and was dissipating gradually. The TWC shown in Fig. 8 was less than 0.1 g cm^{-3}. We could not observe the vertical structure of the cloud with the ground-based observation. Gayet et al. (2009) observed the vertical structure of mixed-phase clouds near Ny-Ålesund, and also found a case where the LWC in the lower part of the cloud was less than 0.1 g cm^{-3}.

Both water droplets and ice particles are present at all times; however, mixing ratios change with time (Fig. 9). The relative contribution of water droplets to

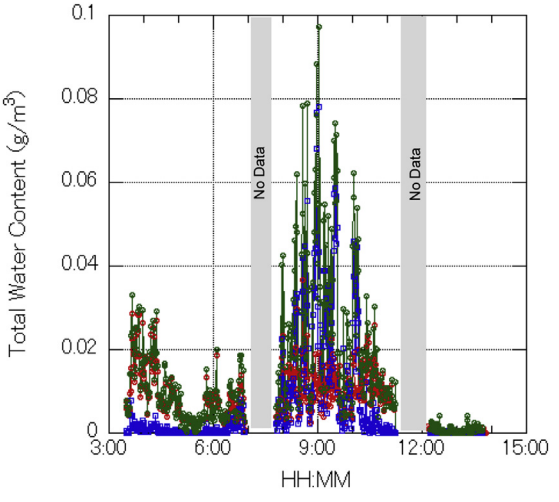

Fig. 8. Liquid water content (LWC) and ice water content (IWC). Red symbols are LWC, and blue IWC. Green symbols are total water content (TWC). (For interpretation of the references to color in this figure legend, the reader is referred to the web version of this article.)

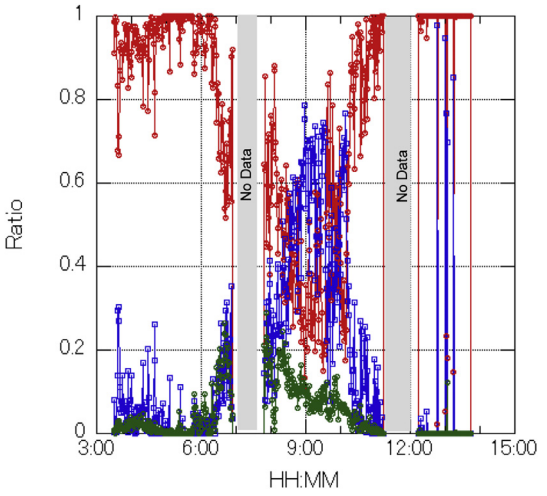

Fig. 9. Relative contribution of particle type to TWC. Red symbols are for water droplets, blue for column-type ice, and green for aggregate-type ice. (For interpretation of the references to color in this figure legend, the reader is referred to the web version of this article.)

the TWC was high in the period when the TWC was relatively low. As the TWC increased, the relative contribution by water droplets decreased and the contribution by ice particles increased. In the period between 08:30 and 10:00, the contribution of water droplets was 0.2–0.3, whereas that of ice particles maximized between 0.7 and 0.8. In this period, cloud layer stably existed; the CBH and the lidar signal were almost constant. This was also the period of maximum TWC. Following this, the contribution of water droplets rose again, becoming nearly 100%.

The contribution of column-type particles to the TWC was dominant, maximizing in the period between 08:30 and 10:00 with values from 0.6 to 0.75. In the period of increased TWC, the contribution of aggregate-type particles to the TWC was also dominant. However, ice particles remained small in this stage. Therefore, there is a possibility that small, column-type particles were classified as aggregated types.

The liquid fraction is defined as fl = LWC/(LWC + IWC). In prior studies (Cober et al., 2001; Korolev et al., 2003; McFarquhar et al., 2007), values of fl of mixed-phase clouds were typically $fl < 0.2$ or $fl > 0.8$, and values in between were relatively few; i.e., clouds are dominated either by liquid or by ice. In our study, fl was dependent on cloud stage.

Fig. 10 shows the water content of every particle type with size ≥75 μm. The contribution of the column type to the TWC is largest. This was caused by columnar particles that grew in size. Fig. 11 portrays

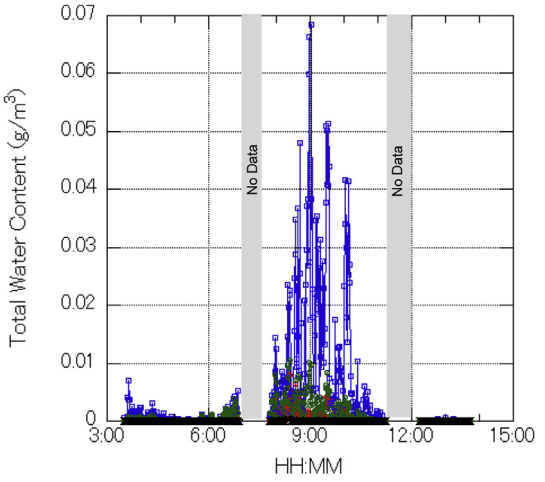

Fig. 10. Particle-type contributions to TWC (particle size ≥75 μm). Red, blue, green, and black symbols are for water droplets, column-type ice, aggregate-type ice and others, respectively. (For interpretation of the references to color in this figure legend, the reader is referred to the web version of this article.)

the relative contributions of particle type to number density. The contribution of ice particles to number density was noisy in the period of low TWC, owing to the low number of densities. In the period of low TWC, the contribution of the aggregate type to number density is greater than that of the column type. In other periods, those of both column and aggregate types are roughly equal. It is notable that there were spherical particles ≥75 μm with a contribution to number

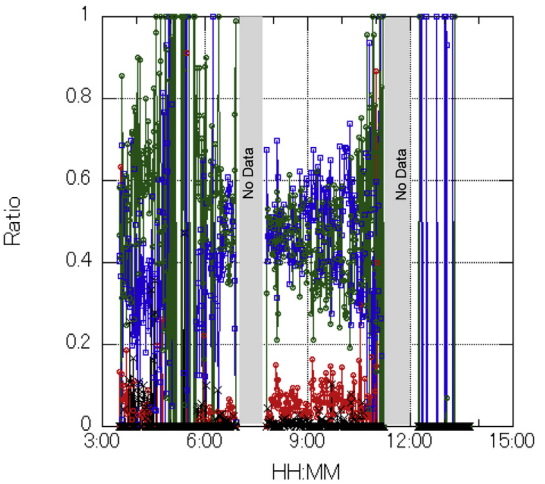

Fig. 11. Contribution of particle types to number density (particle size ≥75 μm). Colors of symbols are same as in Fig. 10. (For interpretation of the references to color in this figure legend, the reader is referred to the web version of this article.)

density from 5% to 10%. Unclassified particles were few in number.

Fig. 12 (a) and (b) shows temporal variation of the number density of water droplets and ice particles. Fig. 13 illustrates the relative contributions of particle type to number density. In every period of the mixed-phase cloud, the contribution of water droplets to number density is large. Generally, the ice particle contribution to number density was less than 10%. In the period of low TWC, the number density of water droplets was 1–3 cm^{-3}, and that of ice particles was less than 0.01 cm^{-3} (10 l^{-1}). In the period of increased and maximized TWC (08:00 through 10:00), the number density of water droplets was 0.5–1.5 cm^{-3}. That of ice particles was 0.05–0.2 cm^{-3} (50–200 l^{-1}) in the period of increased TWC, and 0.01–0.05 cm^{-3} (10–50 l^{-1}) in the period of maximized TWC (08:30 through 10:00). In the period of decreased TWC, the number density of water droplets was 1–3 cm^{-3}. Compared with the results of Gayet et al. (2009) with average mean water droplet density of 40 cm^{-3} and ice particle concentration of 5 l^{-1}, our number densities of water droplets are low and those of ice particles high.

Fig. 14 shows the effective radii of water droplets and effective diameters (size) of ice particles. The effective radius (Hansen and Travis, 1974) is calculated by using CAPS–CAS data for a particle radius ≥2 μm. Effective ice particle diameter is calculated by using CAPS–CIP projected area and volume data for a particle size ≥75 μm (Foot, 1988; Francis et al., 1994; Fu, 1996). In the period of low and increased TWC (06:00–9:00), water droplet effective radius increased from 6 to 15 μm. In the period of maximized TWC (09:00–10:00), it was 11–13 μm. In the period of decreased TWC, it decreased from 12 to 9 μm. Ice particle effective diameter was less than 50 μm in the period of low TWC (before 07:00). In the period of increased and maximized TWC, it increased gradually to a maximum size of 125 μm (07:00–09:30). Thereafter, it gradually declined (09:30–11:30).

4.3. Particle size distribution

Fig. 15 presents the time series of particle size spectra in 30-minute averages. All spectra are shown to illustrate their change. There are three distinctive peaks. We believe that these peaks indicate different particle components. The peaks around the radius of 0.4 and 10 μm correspond to aerosols and cloud water particles, respectively. The peak at around 100 μm corresponds to ice cloud particles, but also includes large water droplets.

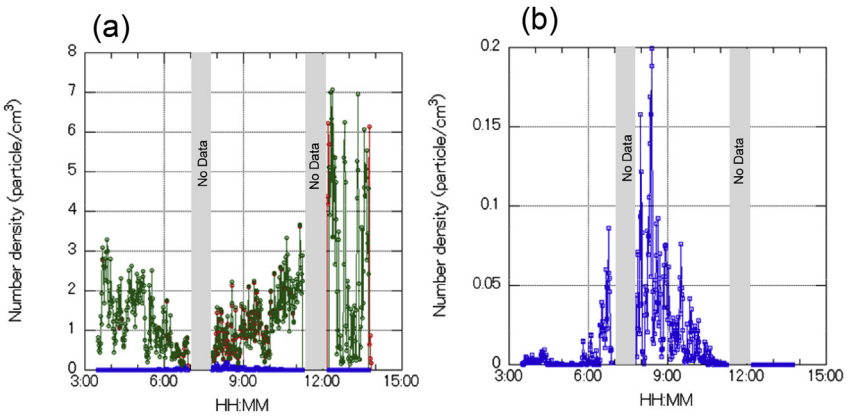

Fig. 12. (a) Number density of water droplets and ice particles, and (b) number density of ice particles. Red symbols are for water droplets, blue for ice particles, and green for total particles. (For interpretation of the references to color in this figure legend, the reader is referred to the web version of this article.)

As seen in Fig. 8, the TWC increased gradually from around 06:00 followed by some variation, and maximized at around 09:00. Thereafter, the TWC decreased gradually. In the period around 06:00, we had precipitation and ice particles fell out of the cloud layer. Therefore, the concentration of particles greater than 75 μm was low. However, number densities between 1 and 10 μm were high; water droplet size was smaller, and there were few ice particles. In the period between 06:00 and 07:30, the size of water droplets increased and the concentration of ice particles began to increase.

Thereafter, water droplet size continued increasing, while the ratio of ice particles increased gradually. At that time, although aerosol size was larger, their growth into cloud particles ceased and the number densities between the radii of 1 and 10 μm dropped.

Following this stage, the ratio of ice particles maximized, as did the water droplet size. At that time, number densities from 1 to 10 μm minimized. In this period, between 08:30 and 10:00, MPL data showed that the precipitation stopped, that the dense lower cloud layer was well spread, and that the CBH was constant.

Thereafter, the ratio of ice particles decreased, water droplet sizes shrank, and number densities from 1 to 10 μm increased. In this period, MPL data showed that the

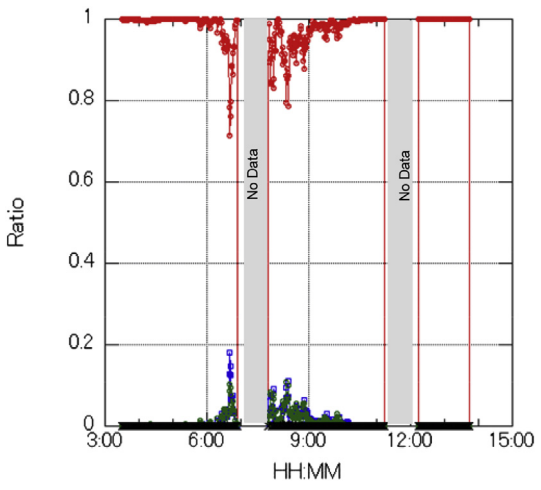

Fig. 13. Contribution of particle types to number density. Colors of symbols are same as in Fig. 10. (For interpretation of the references to color in this figure legend, the reader is referred to the web version of this article.)

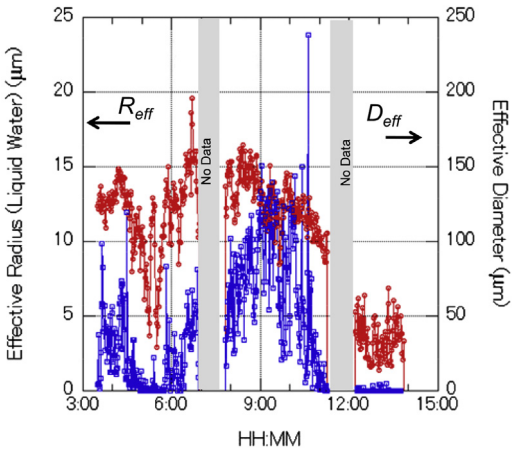

Fig. 14. Effective radii (R_{eff}, red symbols) of water droplets and effective diameters (D_{eff}, blue symbols) of ice particles. R_{eff} was calculated from CAPS–CAS data for ≥2 μm radius. D_{eff} was calculated from particle volume and area data measured by CAPS–CIP. (For interpretation of the references to colour in this figure legend, the reader is referred to the web version of this article.)

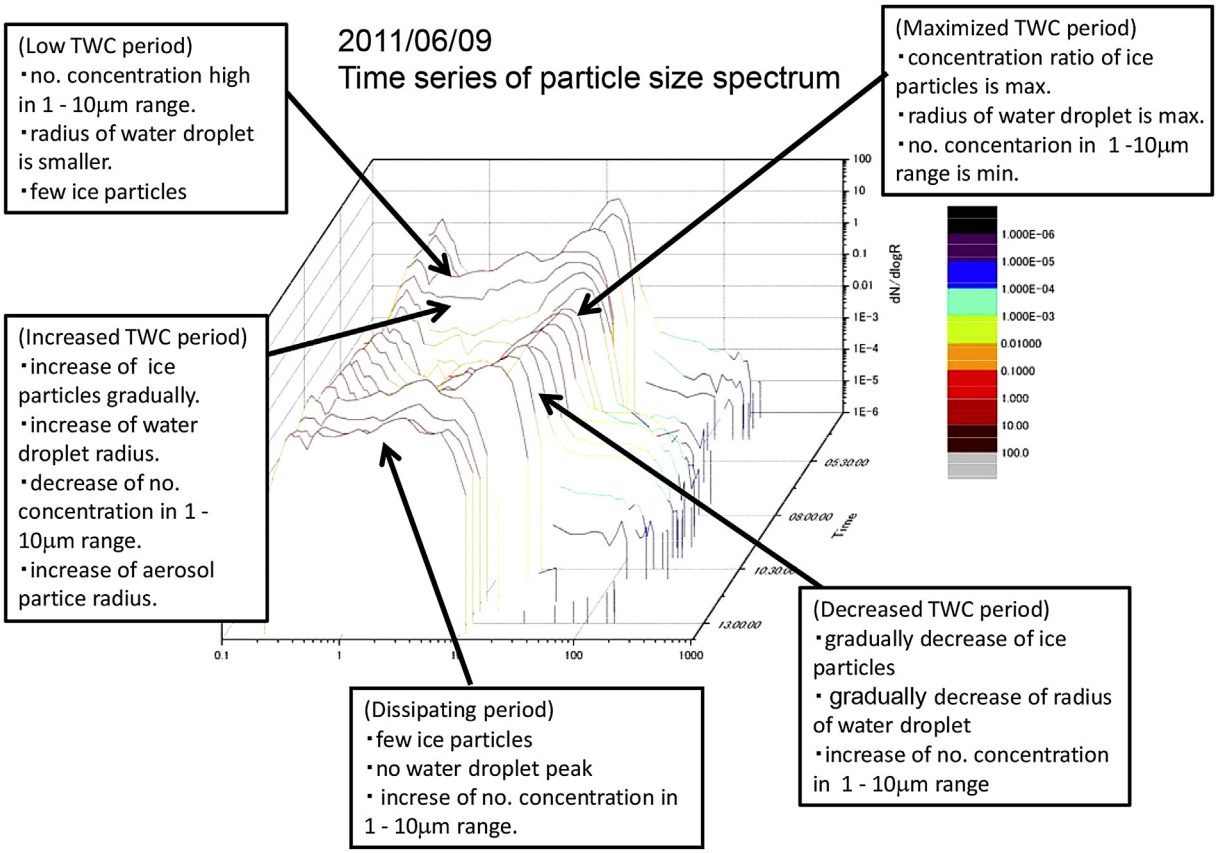

Fig. 15. Time series of particle size spectra (30-minute averages). All size spectra are shown. Particle size spectra throughout the cloud process may be seen.

CBH was lifting gradually and that the cloud layer was becoming scattered. Following this period, ice particles vanished, as did the number density peak for water droplets. Furthermore, number densities for particle sizes between radii of 1−10 μm increased. In this period, the CBH rose above the Zeppelin station. After about 14:30, MPL data showed that the cloud layer had dissipated.

4.4. Optical properties

Optical properties of clouds are important parameters for the earth radiation budget and remote sensing techniques. Therefore, to investigate the optical properties of mixed-phase clouds, single-scattering properties (extinction, absorption coefficients, single-scattering albedo (SSA), and asymmetry factors) were derived. These were based on the database of Yang et al. (2000), using the parameters extracted from the measured image. Yang et al. (2000) computed single-scattering properties of ice crystals with various shapes and sizes in 56 narrow spectral bands from 0.2 to 5 μm. Given the optical properties of individual particles, the optical properties of the cloud are calculated by weighting the size distribution of particles for each particle type.

The following results were obtained (figures not shown).

1) Wavelength dependence of extinction coefficients was small.
2) Wavelength dependence of absorption coefficients was caused mainly by that of the imaginary part of the refractive index.
3) With IWC variation, the contribution of ice particles to absorption coefficients was sensitive to IWC, largely around the wavelengths of 1.6 and 2.2 μm.
4) Change of asymmetry factor was slight at every wavelength.

The above results show the possibility of using the wavelength regions of 1.6 and 2.2 μm in the field of remote sensing, because SSA differences between water droplets and ice particles are small at wavelengths below

1.3 μm. There are also gas absorption bands in the wavelength regions of 1.4 and 1.9 μm. This is well known and satellites already have sensors at 1.6 and 2.2 μm bands. Examples are the Moderate Resolution Imaging Spectroradiometer (MODIS; King et al., 1992) and Global Imager (Nakajima et al., 1998).

Fig. 16 shows the time series of SSA and asymmetry factor at wavelengths of 500, 1575, and 2250 nm. Values for water droplets, ice particles, and total particles are shown. The influence of the water droplets and ice particles on SSA and asymmetry factor is dependent on wavelength.

The SSA at 500 nm is 1.0, because there is no absorption of water and ice within the visible wavelength region. The influence of water and ice particles on SSA at 1.6 μm is greater than that at 2.2 μm. Differences between water droplets and total particles at 1575 nm are at most about 0.05, even during periods when the relative contribution of ice particles to TWC was at the maximum. However, the SSA variation of water droplets at 1575 nm was small: less than 0.05 during all observation periods. Therefore, by using the radiance at a wavelength of around 1.6 μm, it is possible that information on LWC and IWC can be obtained.

The difference of asymmetry factor between water droplets and ice particles was great at a wavelength of 550 nm, and small at 1575 and 2250 nm. From polar nephelometer measurements at 804 nm, Gayet et al. (2002) showed that water droplets have typical values of asymmetry factor >0.8, and ice particles have lower values. However, in our case study, this factor for total particles was close to that of water droplets. Therefore, pure ice cloud may be distinguished from water and mixed-phase cloud, but it is difficult to obtain information on water droplets and ice particles. In any case, optical properties are determined mainly by those of liquid water particles.

5. Summary and conclusion

In May and June 2011, in situ measurements of mixed-phase boundary layer clouds were made at the Norwegian Polar Institute Zeppelin Station in Ny-Ålesund (78.9°N, 11.9°E), Svalbard. The instruments consisted of a CAPS, PVM-100 and CPM. The CAPS comprised a CAS and CIP. These instruments were installed atop the roof of the station, which is on the ridge of Mt. Zeppelin at an altitude of 474 m. The

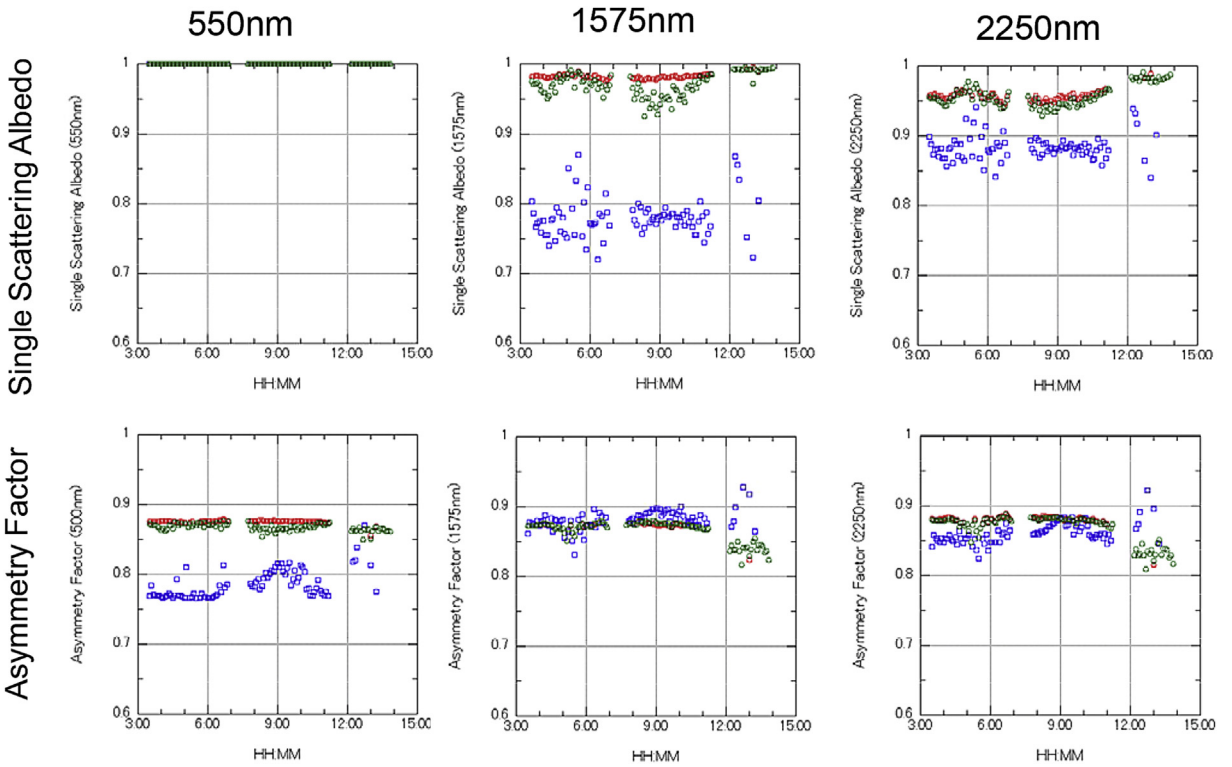

Fig. 16. Time series of optical properties (single-scattering albedo and asymmetry factor). Red, blue, and green symbols are for water droplets, ice particles, and total particles (water droplets + ice particles). Upper panels are single scattering albedo and lower ones are asymmetry factor. (For interpretation of the references to colour in this figure legend, the reader is referred to the web version of this article.)

vertical structure of clouds could not be measured by the ground-based instruments. Nevertheless, long-term continuous measurements were made, and we could observe various stages of cloud microphysics.

During the observation period, clouds were observed associated both with cyclonic disturbances and with outbreaks of westerly cold air from the sea. Atmospheric temperature and relative humidity during all measurements were from 0 to −5 °C and 90 to 100%, respectively. We analyzed data measured by the CAPS–CAS and CSPS–CIP. These acquired size spectra in the diameter range 0.35–1550 μm.

New software for analyzing the CAPS–CIP data was developed. Elliptical shapes were assumed in the particle image analysis. Particle classification was performed by using the following parameters: (1) axis ratio (*a*/*b*); (2) perimeter ratio (*Lp*/*Lc*); and (3) difference of perimeter (*Lcol*/*Lc* − *Lp*/*Lc*). Particles were classified as spheres, columns, aggregates, and others.

Measured size spectra of cloud particles less than 25-μm radius were substantially different from those with greater radii. The former correspond to water droplets and the latter are attributable mainly to ice particles. Measured spectra changed with time. The ratio of water droplets to ice particles depended on the cloud stage; clouds were not dominated either by liquid or by ice except during the period of lower TWC, which may correspond to the early and dissipative stages of cloud development. TWC was low, less than 0.1 g/m^3. In the period when the cloud was dense and stable, which may correspond to the mature stage of cloud development, the contribution of water droplets to the TWC was 0.2–0.3, and that of ice particles was 0.7–0.8.

The particle classification results showed that the dominant ice particles are of column-type. There were spherical particles (water droplet) with radii of $\geq$ 75 μm. The number density of water droplets was 5–10% of the total number of particles with radii of $\geq$ 75 μm.

In all periods, the predominant cloud particles were water droplets. The number density of droplets was between 0.5 and 1.5 cm^{-3} in the period of increased and maximized TWC. The number density of ice particles varied with stage. In the period of increased TWC, this was 50–200 l^{-1}, and it was 10–50 l^{-1} in the period of maximized TWC. Compared with a previous study, the number density of water droplets was low and that of ice particles high.

The effective radii of water droplets and effective diameters of ice particles varied with cloud stage. In the period of low and increased TWC, effective water droplet radii increased from 6 to 15 μm; in the period of maximized TWC, they were 11–13 μm. Effective diameters of ice particles increased gradually to a maximum size of 125 μm in the period of maximized TWC.

We obtained particle size spectra of the cloud via continuous observation. Time series of particle size spectra changed with cloud stage. This variation of size spectra revealed the growth of aerosol particles into water droplets and the growth of water into ice particles, and vice versa.

Extinction and absorption coefficients, SSA, and asymmetry factors were calculated based on measured cloud microphysics, using the dataset of Yang et al. (2000).

Optical properties were determined mainly by those of liquid water particles, even during periods when the relative contribution of ice particles to TWC was at the maximum. Dependence of IWC on absorption coefficients was evident at wavelengths greater than 1.0 μm. The contribution of ice particles to absorption coefficients changed substantially around wavelengths of 1.6 and 2.2 μm. The wavelength region of 1.6 and 2.2 μm can be used in remote sensing. The possibility that the LWC and IWC of mixed-phase clouds can be retrieved by combining 1.6 and 2.2 μm data was confirmed.

Acknowledgments

We are very grateful to the staff of the Norwegian Polar Institute and Norwegian Institute for Air Research at Zeppelin Station for their cooperation in the field experiments during May and June 2011. We also very grateful to Alfred Wegener Institute for permission to use the meteorological and radiosonde data. The authors are also very grateful to Prof. P. Yang for permission to use his database on single-scattering properties of ice particles. We also express our appreciation to two anonymous reviewers for their useful comments. This study was supported partially by Japan Society for the Promotion of Science (JSPS) Grants-in-Aid for Scientific Research (Nos. 21403006 and 22310015).

References

Auer Jr., A.H., Veal, D.L., 1970. The dimension of ice crystals in natural clouds. J. Atmos. Sci. 27, 919–926.

Baumgardner, D., Jonsson, H., Dawson, W., O'Connor, D., Newton, R., 2002. The cloud, aerosol and precipitation spectrometer: a new instrument for cloud investigations. Atmos. Res. 59–60, 251–264.

Boudala, F.S., Isaac, G.A., Fu, Q., Cober, S.G., 2002. Parameterization of effective ice particle size for high-latitude clouds. Int. J. Climatol. 22, 1267–1284.

Brock, C.A., Cozic, J., Bahreini1, R., Froyd, K.D., Middlebrook, A.M., McComiskey, A., Brioude, J., Cooper, O.R., Stohl, A., Aikin, K.C., de Gouw, J.A., Fahey, D.W., Ferrare, R.A., Gao, R.-S., Gore, W., Holloway, J.S., Hübler, G., Jefferson, A., Lack, D.A., Lance, S., Moore, R.H., Murphy, D.M., Nenes, A., Novelli, P.C., Nowak, J.B., Ogren, J.A., Peischl, J., Pierce, R.B., Pilewskie, P., Quinn, P.K., Ryerson, T.B., Schmidt, K.S., Schwarz, J.P., Sodemann, H., Spackman, J.R., Stark, H., Thomson, D.S., Thornberry, T., Veres, P., Watts, L.A., Warneke, C., Wollny, A.G., 2011. Characteristics, sources, and transport of aerosols measured in spring 2008 during the aerosol, radiation, and cloud processes affecting Arctic climate (ARCPAC) project. Atmos. Chem. Phys. 11, 2423–2453. http://dx.doi.org/10.5194/acp-11-2423-2011. www.atmos-chem-phys.net/11/2423/2011/.

Campbell, J.R., Shiobara, M., 2008. Glaciation of a mixed-phase boundary layer cloud at a coastal arctic site as depicted in continuous lidar measurements. Polar Sci. 2, 121–127. http://dx.doi.org/10.1016/j.polar.2008.04.004.

Cober, S.G., Isaac, G.A., Korolev, A., Strapp, J.W., 2001. Assessing cloud-phase conditions. J. Appl. Meteorol. 40, 1967–1983.

Curry, J.A., Rossow, W.B., Randall, D., Schramm, J.L., 1996. Overview of arctic cloud and radiation characteristics. J. Clim. 9, 1731–1764.

Curry, J.A., Hobbs, P.V., King, M.D., Randall, D.A., Minnise, P., Isaac, G.A., Pinto, J.O., Uttal, T., Bucholtz, A., Cripe, D.G., Gerber, H., Fairall, C.W., Garrett, T.J., Hudson, J., Intrieri, J.M., Jakob, C., Jensen, T., Lawson, P., Marcotte, D., Nguyen, L., Pilewskie, P., Rangno, A., Rogers, D.C., Strawbridge, K.B., Valero, F.P.J., Williams, A.G., Wyliep, D., 2000. FIRE Arctic clouds experiment. Bull. Amer. Meteor. Soc. 81, 5–29.

Cunningham, M.R., 1978. Analysis of particle spectral data from optical array (PMS) 1D and 2D sensors. In: American Meteorological Society, Fourth Symposium. Meteorological Observation Instruments, Denver, USA, 10–14 April, pp. 345–350.

Foot, J.S., 1988. Some observations of the optical properties of clouds: II cirrus. Q. J. Roy. Meteorol. Soc. 114, 145–164.

Francis, P.N., Jones, A., Saunders, R.W., Shine, K.P., Slingo, A., Sun, Z., 1994. An observational and theoretical study of the radiative properties of cirrus: some results from ICE'89. Q. J. Roy. Meteorol. Soc. 120, 809–848.

Fu, Q., 1996. An accurate parameterization of the solar radiative properties of cirrus clouds for climate models. J. Clim. 9, 2058–2082.

Gayet, J.-F., Mioche, G., Dörnbrack, A., Ehrlich, A., Lampert, A., Wendisch, M., 2009. Microphysical and optical properties of Arctic mixed-phase clouds. The 9 April 2007 case study. Atmos. Chem. Phys. 9, 6581–6595. www.atmos-chem-phys.net/9/6581/2009/.

Gayet, J.-F., Asano, S., Yamazaki, A., Uchiyama, A., Sinyuk, A., Jourdan, O., Auriol, F., 2002. Two case studies of winter continental-type water and mixed-phase stratocumuli over the sea 1. Microphysical and optical properties. J. Geophys. Res. 107 (D21), 4569. http://dx.doi.org/10.1029/2001JD001106.

Gayet, J.-F., Stachlewska, I.S., Jourdan, O., Shcherbakov, V., Schwarzenboeck, A., Neuber, R., 2007. Microphysical and optical properties of precipitating drizzle and ice particles obtained from alternated lidar and in situ measurements. Ann. Geophys. 25, 1487–1497. www.ann-geophys.net/25/1487/2007/.

Gorodetskaya, I.V., Tremblay, L., Liepert, B., Cane, M.A., Cullather, R.I., 2008. The influence of cloud and surface properties on the Arctic Ocean shortwave radiation budget in coupled models. J. Clim. 21, 866–882.

Hansen, J.E., Travis, L.D., 1974. Light scattering in planetary atmosphere. Space Sci. Rev. 16, 527–610.

Heymsfield, A.J., 1972. Ice crystal terminal velocities. J. Atmos. Sci. 29, 1348–1357.

Heymsfield, A.J., Parrish, J.L., 1978. A computational technique for increasing the effective sampling volume of the PMS twodimensional particle size spectrometer. J. Appl. Meteorol. 17, 1566–1572.

Holland, M.M., Serreze, M.C., Stroeve, J., 2008. The sea ice mass budget of the Arctic and its future change as simulated by coupled climate models. Clim. Dynam. 34, 185–200. http://dx.doi.org/10.1007/s00382-008-0493-4.

Inoue, J., Liu, J., Pinto, J., Curry, J., 2006. Intercomparison of Arctic regional climate models: modeling clouds and radiation for SHEBA in May 1998. J. Clim. 19, 4167–4178.

King, M.D., Kaufman, Y.J., Menzel, W.P., Tanré, D., 1992. Remote sensing of cloud, aerosol, and water vapor properties from the Moderate Resolution Imaging Spectrometer (MODIS). IEEE Trans. Geosci. Remote Sens 30, 2–27.

Kolstad, E.W., Bracegirdle, T.J., Seierstad, I.A., 2008. Marine cold air outbreaks in the North Atlantic: temporal distribution and associations with large-scale atmospheric circulation. Clim. Dynam. 33 (2–3), 187–197.

Korolev, A., Isaac, G.A., Cober, S.G., Strapp, J.W., Hallett, J., 2003. Microphysical characterization of mixed-phase clouds. Q. J. Roy. Meteorol. Soc. 129, 39–65.

McFarquhar, G.M., Ghan, S., Verlinde, J., Korolev, A., Strapp, J.W., Schmid, B., Tomlinson, J.M., Wolde, M., Brooks, S.D., Cziczo, D., Dubey, M.K., Fan, J., Flynn, C., Gultepe, I., Hubbe, J., Gilles, M.K., Laskin, A., Lawson, P., Leaitch, W.R., Liu, P., Liu, X., Lubin, D., Mazzoleni, C., Macdonald, A.-M., Moffet, R.C., Morrison, H., Ovchinnikov, M., Shupe, M.D., Turner, D.D., Xie, S., Zelenyuk, A., Bae, K., Freer, M., Glen, A., 2011. Indirect and semi-direct aerosol campaign: the impact of arctic aerosols on clouds. Bull. Amer. Meteor. Soc. 92, 183–201.

McFarquhar, G., Zhang, G., Poellot, M.R., Kok, G.L., Mc-Coy, R., Tooman, T., Fridlind, A., Heymsfield, A., 2007. Ice properties of single-layer stratocumulus during the mixed-phase Arctic cloud experiment. J. Geophys. Res. 112, D24201. http://dx.doi.org/10.1029/2007JD008633.

Mie, G., 1908. Beiträge zur Optik trüber Medien, speziell kolloidaler Metallösungen. Ann. Phys. 25, 377–445.

Mitchell, D.L., Arnott, W.P., 1994. A model predicting the evolution of ice particle size spectra and radiative properties of cirrus clouds, II, dependence of absorption and extinction on ice crystal morphology. J. Atrnos. Sci. 51, 817–832.

Nakajima, T.Y., Nakajima, T., Nakajima, M., Fukushima, H., Kuji, M., Uchiyama, A., Kishino, M., 1998. Optimization of the advanced earth observing satellite II global imager channels by use of radiative transfer calculations. Appl. Opt. 37, 3149–3163.

Perovich, D.K., Andreas, E.L., Curry, J.A., Eiken, H., Fairall, C.W., Grenfell, T.C., Guest, P.S., Intrieri, J., Kadko, D., Lindsay, R.W., McPhee, M.G., Morison, J., Moritz, R.E., Paulson, C.A., Pegau, W.S., Persson, P.O.G., Pinkel, R., Richter-Menge, J.A., Stanton, T., Stern, H., Sturm, M., Tucker III, W.B., Uttal, T., 1999. Year on ice gives climate insights. Eos Trans. AGU 80 (481), 485–486.

Richter, A., Gayet, J.-F., Mioche, G., Ehrlich, A., Dörnbrack, A., 2008. Mixed-phase clouds in the arctic: a synopsis of airborne lidar, in-situ, and albedometer observations, complemented by meteorological analyses. In: 24th International Laser Radar Conference (ILRC) 23−27 June 2008, Boulder, USA, pp. 881−884.

Shiobara, M., Yabuki, M., Kobayashi, H., 2003. A polar cloud analysis based on micro-pulse lidar measurements at Ny-Alesund, Svalbard and Syowa, Antarctica. Phys. Chem. Earth 28, 1205−1212.

Shiobara, M., Yabuki, M., Neuber, R., Spinhirne, J.D., Welton, E.J., Campbell, J.R., Hart, W.D., Berkoff, T.A., 2006. Arctic experiment for ICESat/GLAS ground validation with a micro-pulse lidar at Ny-Alesund, Svalbard. Polar Meteorol. Glaciol 20, 28−39.

Shupe, M.D., Intrieri, J.M., 2004. Cloud radiative forcing of the Arctic surface: the influence of cloud properties, surface albedo, and solar zenith angle. J. Clim. 17, 616−628. http://dx.doi.org/10.1175/1520-0442(2004)017<0616:CRFOTA>2.0.CO;2.

Shupe, M.D., Matrosov, S.Y., Uttal, T., 2006. Arctic mixed-phase cloud properties derived from surface-based sensors at SHEBA. J. Atmos. Sci. 63, 697−711. http://dx.doi.org/10.1175/JAS3659.1.

Shupe, M.D., Walden, V.P., Eloranta, E., Uttal, T., Campbell, J.R., Starkweather, S.M., Shiobara, M., 2011. Clouds at arctic atmospheric observatories. Part I: occurrence and macrophysical properties. J. Appl. Meteor. Climatol. 50, 626−644.

SEARCH SSC, 2001. SEARCH: Study of Environmental Arctic Change, Science Plan, 2001. Polar Science Center, Applied Physics Laboratory, University of Washington, 89 pp.

Solomon, S., Qin, D., Manning, M., Marquis, M., Averyt, K., Tignor, M.M.B., Miller Jr., H.L., Chen, Z., 2007. Climate change 2007. In: The Physical Science Basis. Cambridge University Press, 996 pp.

Tunved, P., Ström, J., Krejci, R., 2013. Arctic aerosol life cycle: linking aerosol size distributions observed between 2000 and 2010 with air mass transport and precipitation at Zeppelin station, Ny-Ålesund, Svalbard. Atmos. Chem. Phys. 13, 3643−3660. http://dx.doi.org/10.5194/acp-13-3643-2013. www.atmos-chem-phys.net/13/3643/2013/.

Verlinde, J., Harrington, J.Y., Mcfarquhar, G.M., Yannuzzi, V.T., Avramov, A., Greenberg, S., Johnson, N., Zhang, G., Poellot, M.R., Mather, J.H., Turner, D.D., Eloranta, E.W., Zak, B.D., Prenni, A.J., Daniel, J.S., Kok, G.L., Tobin, D.C., Holz, R., Sassen, K., Spangenberg, D., Minnis, P., Tooman, T.P., Ivey, M.D., Richardson, S.J., Bahrmann, C.P., Shupe, M., Demott, P.J., Heymsfield, A.J., Schofield, R., 2007. The mixed-phase arctic clouds experiment. Bull. Amer. Meteor. Soc. 88, 205−221.

Yamanouchi, T., Treffeisen, R., Herber, A., Shiobara, M., Yamagata, S., Hara, K., Sato, K., Yabuki, M., Tomokawa, Y., Rinke, A., Neuber, R., Schumachter, R., Kriews, M., Ström, J., Schrems, O., Gernandt, H., 2005. Arctic study of Tropospheric aerosol and radiation (ASTAR) 2000: arctic haze case study. Tellus 57B, 141−152.

Yang, P., Liou, K.N., Wyser, K., Mitchell, D., 2000. Parameterization of scattering and absorption properties of individual ice crystals. J. Geophys. Res. 105, 4699−4718.

Zuidema, P., Baker, B., Han, Y., Intrieri, J., Key, J., Lawson, P., Matrosov, S., Shupe, M., Stone, R., Uttal, T., 2005. An Arctic springtime mixed-phase cloudy boundary layer observed during SHEBA. J. Atmos. Sci. 62, 160−176. http://dx.doi.org/10.1175/JAS-3368.1.